Photothermal optical coherence tomography in *ex vivo* human breast tissues using gold nanoshells

Chao Zhou,[1] Tsung-Han Tsai,[1] Desmond C. Adler,[1,2] Hsiang-Chieh Lee,[1] David W. Cohen,[3] Amy Mondelblatt,[3] Yihong Wang,[3] James L. Connolly,[3] and James G. Fujimoto[1,*]

[1]*Department of Electrical Engineering and Computer Science and Research Laboratory of Electronics, Massachusetts Institute of Technology, 77 Massachusetts Avenue, Cambridge, Massachusetts 02139, USA*

[2]*LightLab Imaging, Inc., Westford, Massachusetts 01886, USA*

[3]*Department of Pathology, Beth Israel Deaconess Medical Center, Harvard Medical School, Boston, Massachusetts 02215, USA*

**Corresponding author: jgfuji@mit.edu*

Received November 9, 2009; accepted December 14, 2009;
posted January 12, 2010 (Doc. ID 119569); published February 25, 2010

We demonstrate photothermal optical coherence tomography (OCT) imaging in highly scattering human breast tissue *ex vivo*. A 120 kHz axial scan rate, swept-source phase-sensitive OCT system at 1300 nm was used to detect phase changes induced by 830 nm photothermal excitation of gold nanoshells. Localized phase modulation was observed 300–600 μm deep in scattering tissue using an excitation power of only 22 mW at modulation frequencies up to 20 kHz. This technique enables integrated structural and molecular-targeted imaging for cancer markers using nanoshells. © 2010 Optical Society of America

OCIS codes: 110.4500, 190.4870, 160.4236, 170.4730, 170.6930.

Optical coherence tomography (OCT) is a powerful tool for assessing tissue architectural morphology [1]. It enables three-dimensional (3D) imaging with resolutions approaching that of histopathology but can be performed *in vivo* and in real time without the need to remove and process specimens. Conventional OCT imaging is based on contrast from spatial variations in tissue scattering. The use of exogenous contrast agents would allow targeted imaging of specific cells, receptors, or functional processes. OCT contrast enhancement has been demonstrated using scattering microspheres [2], iron oxide microparticles [3], and nanoparticles [4–10]. Gold nanoparticles are attractive for OCT owing to their customizable absorption and scattering properties, biocompatibility, and ease of conjugation to antibodies and peptides that bind selectively with proteins associated with specific diseases [11]. Gold nanoparticles have also been used as photothermal therapy agents [12,13]. These characteristics offer gold nanoparticles "three-in-one" [14] functionality as targeting probes, image contrast enhancers, and therapeutic agents.

Our group demonstrated phase-sensitive OCT to detect gold nanoshells as contrast agents in phantoms with high signal-to-noise ratio (SNR) [9]. The technique uses nanoshells with absorption at 780 nm, where tissue absorption is inherently low. An excitation laser at 808 nm induces small temperature gradients in sample regions containing nanoparticles. These thermal variations modulate the sample's optical path length, which is detected using phase-sensitive OCT. Photothermal OCT selectively detects regions containing nanoshells, potentially enabling molecular contrast. Other groups working in parallel demonstrated photothermal OCT imaging in 3D cell constructs using immunotargeted gold nanospheres [10]. Photothermal OCT imaging is challenging in tissues where scattering plays an important role. In this Letter, we demonstrate the feasibility of photothermal OCT in human breast tissue. By modulating the thermal excitation beam at high frequencies, localized photothermal phase contrast can be observed 300–600 μm deep in a tissue using a photothermal modulation power of only 22 mW at 830 nm.

A swept-source OCT system (Fig. 1) with a buffered Fourier-domain mode-locked (FDML) laser running at 1310 nm and 120 kHz was used for these studies. The laser tuning range is ~170 nm. Photothermal excitation was performed with an 830 nm single mode laser diode. Gold nanoshells (Nanospectra Biosciences Inc.) with a peak absorption cross-section at 780 nm ($\sim 4\times 10^{-10}$ cm^2) consisting of a 120 nm silica core and a 16 nm gold shell were used. The absorption cross-section is $\sim 3\times 10^{-10}$ cm^2 at 1310 nm [15]. Combining the 1310 and 830 nm light into the same fiber enables the photothermal modulation beam and the OCT imaging beam to maintain alignment during scanning. The combined beam was scanned with a galvanometer on the tissue. The $1/e^2$ spot size was measured to be 25 and 30 μm for 830 and 1310 nm, respectively. The axial resolution was ~8 μm in tissue. The phase detection sensitivity was measured using an isolated reflector in the sample arm. The phase variation between consecutive A-lines was

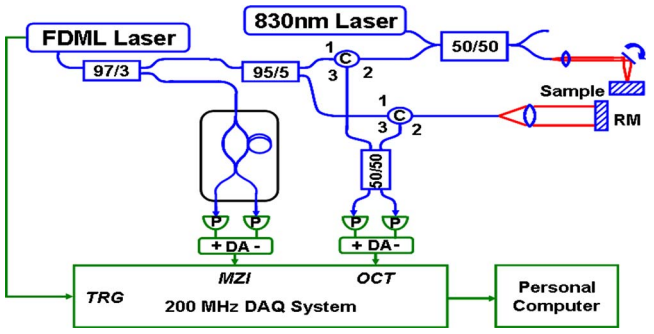

Fig. 1. (Color online) Schematic of photothermal OCT setup. A collinear photothermal excitation beam is coupled into a swept source OCT imaging system.

measured at the peak reflection position, and the standard deviation was ~5 mrad. The average photothermal power on the sample was 22 mW with a sine wave modulation at various frequencies (5, 10, and 20 kHz). The reflected 830 nm light is blocked by the 1310 nm circulator and does not affect the OCT signal. The small photothermal spot size enables lower power to be used and the exposed area to cool at a faster rate compared to our previous phantom experiment [9].

To simulate the accumulation of molecular-targeted nanoshells in pathological tissues, less than 50 μl of 5×10^9 ml^{-1} bare gold nanoshell solution was injected into freshly excised human breast tissue collected from reduction mammoplasty specimens. This concentration is consistent with the estimated concentration attainable in tumor tissues [6]. The collected tissue was "discarded tissue" and not necessary for pathologic diagnosis. Microscopically the discarded tissue was comprised of fibrofatty tissue with benign breast lobules (terminal duct lobular unit). The protocol was approved by the IRB at Massachusetts Institute of Technology, and BIDMC. We appreciate that the use of *ex vivo* specimens are imperfect approximations to *in vivo* imaging; however, it serves to demonstrate the feasibility of these imaging methods in scattering tissue. Photothermal OCT was performed near the nanoshell injection sites with the OCT beam focused ~500 μm below the tissue surface. An OCT signal along with a calibration Mach–Zhender interferometer (MZI) signal was continuously acquired using a 14 bit, 200 MHz A/D converter. 1667 sample points were acquired per frequency sweep, and a chirped Z transform was used to obtain amplitude and phase profiles within the top 800 μm imaging range with 1024 points for each A-scan. The data were acquired over a transverse distance of 2 m across the tissue with various scanning speeds from 2 to 16 mm/s.

Time-dependent phase curves at each sample depth were obtained over 234 transverse A-lines [~2 ms acquisition, Fig. 2(d)]. A low-frequency background phase drift was removed using a sixth-order polynomial fit before a transverse spatial fast Fourier transform (FFT) was performed to generate phase modulation spectra as a function of frequency. Spectra from four consecutive depth pixels were averaged to reduce noise [Fig. 2(e)]. First, the phase modulation amplitude at the photothermal modulation frequency (5, 10, or 20 kHz) was extracted. The background phase noise level was then obtained by averaging the signal amplitude at frequencies 1 to 2 kHz higher than the photothermal modulation frequency. A photothermal image was constructed by subtracting the background from the phase modulation amplitude. An SNR image was then obtained by normalizing the photothermal image to the standard deviation of signal in a nanoshell-free region. An SNR threshold of 4 and an OCT intensity threshold of −40 dB were used to isolate regions containing photothermal signals, which were superimposed as pseudocolor on the gray scale structural OCT images. A 5×5 pixel mean filter was used to smooth the image. Images obtained without photothermal modulation and from a saline injected specimen were used as controls.

As shown in Figs. 2(b) and 2(c), photothermal OCT can visualize localized accumulation of nanoshells near the injection site ~300–600 μm below the tissue surface. Phase modulation was absent in the saline injection controls [Fig. 2(a)] or when there was no photothermal excitation. In addition, as the modulation frequency increases from 5 to 10 kHz, the photothermal SNR increases from ~16 to 24 measured at locations marked X in Fig. 2(c), although the amplitude of the phase modulation decreases from 10.8 to 6.5 (arbitrary unit). Modulating at higher frequencies allows a lower photothermal modulation signal

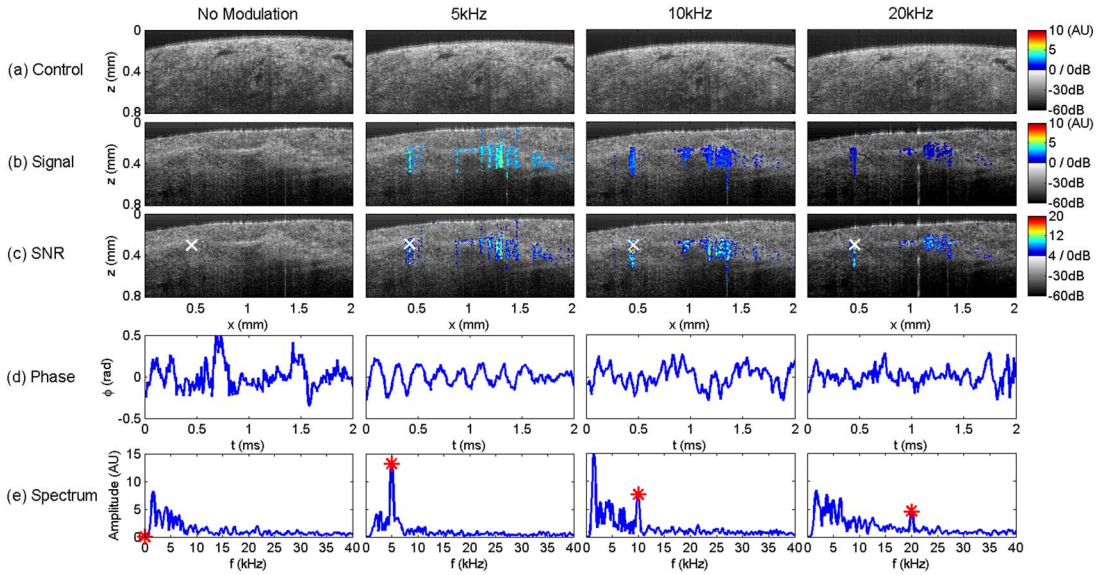

Fig. 2. (Color online) Photothermal OCT in human breast tissues *ex vivo*. (a) No photothermal signal is observed from control images in saline injected specimen. (b) Phase modulation signal and (c) SNR images from the nanoshell injected specimen (no excitation, 5, 10, and 20 kHz modulation) demonstrate localized photothermal signal. (d, e) Time-dependent phase modulation and frequency spectra corresponding to pixels marked in (c).

to be detected with a relatively high SNR, because the phase noise is lower. Increasing the modulation frequency to 20 kHz results in a SNR of ~23, although the phase modulation signal decreases to 3.5. The peak-to-peak phase change is only ~0.1 rad for the 20 kHz modulation [Fig. 2(d)], corresponding to an optical path length change of ~20 nm. Figure 3 shows images of the phase modulation signal at scan speeds of 2–16 mm/s using 10 kHz photothermal modulation. The same threshold was used to determine regions where nanoshells were present. The phase modulation from nanoshell thermomodulation can be visualized at a beam-scanning speed of 16 mm/s.

These results demonstrate that photothermal OCT is feasible in highly scattering tissues. In scattering samples, one of the major sources of phase noise is from the microstructural features in the tissue. Interference speckle also contributes to the background phase noise. However, the influence from these sources is mainly at low frequency. In addition, the scattering of the thermal excitation beam results in a larger volume of heated tissue. This reduces the temperature/phase changes within the focal volume and makes the modulated phase signal smaller and harder to detect. In this study, several approaches were used to improve the photothermal phase signal SNR. The most significant is to modulate and detect the phase signal at a high frequency. The photothermal modulation frequency employed here (5, 10, and 20 kHz) is much higher than the frequency used previously (e.g., 25 Hz) [10]. The $1/f$ background phase noise is reduced at frequencies away from the base band, improving the SNR. Modulation at a higher frequency also improves imaging speed. Previous studies suggest that an optimal photothermal modulation frequency exists for a given sample and imaging system to achieve sufficient detection sensitivity [9]. This is critical for *in vivo* applications where the agent may be administered systemically and local concentrations are low.

These results also demonstrated that photothermal detection is possible at low power levels, consistent with future *in vivo* applications. This is achieved by combining the thermal modulation and OCT imaging beam into the same optical fiber, focusing to a tight spot. Compared to previous experiments [9], this significantly reduced the photothermal spot size, which reduces excitation energy required to generate a strong local phase modulation. The smaller focal volume also has a rapid thermal relaxation time, minimizing local heat accumulation in the sample.

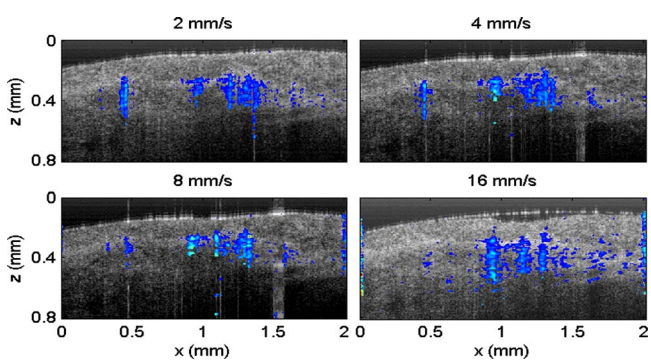

Fig. 3. (Color online) Phase-modulation signal images at various beam-scanning speeds ranging from 2 to 16 mm/s with 10 kHz photothermal modulation.

One limitation of photothermal OCT is that a high oversampling (>100 transverse samples per beam diameter at 16 mm/s scanning speed) is needed to extract the phase modulation signal, limiting the imaging speed. This can be mitigated by acquiring fewer transverse samples (N) at a cost of reduced SNR (scaled as the square root of N). A balance exists between optimizing the imaging speed and signal contrast. Another limitation of the current study is that unconjugated nanoshells were used to simulate the localized accumulation of the contrast agent. In future studies, we will investigate antibody fragment or peptide marker conjugated nanoshells for molecularly targeted imaging.

This work was supported by the NIH grant R01-CA75289-13, AFOSR contract FA9550-07-1-0014, and MFELP contract FA9550-07-1-0101. D. C. Adler acknowledges Canadian support from NSERC and the Heritage Scholarship Fund. T. H. Tsai acknowledges support from the CIMIT and the Taiwan Merit Scholarship from the NSCT.

References

1. D. Huang, E. A. Swanson, C. P. Lin, J. S. Schuman, W. G. Stinson, W. Chang, M. R. Hee, T. Flotte, K. Gregory, C. A. Puliafito, and J. G. Fujimoto, Science **254**, 1178 (1991).
2. T. M. Lee, A. L. Oldenburg, S. Sitafalwalla, D. L. Marks, W. Luo, F. J. J. Toublan, K. S. Suslick, and S. A. Boppart, Opt. Lett. **28**, 1546 (2003).
3. A. L. Oldenburg, J. R. Gunther, and S. A. Boppart, Opt. Lett. **30**, 747 (2005).
4. C. Loo, A. Lin, L. Hirsch, M. H. Lee, J. Barton, N. Halas, J. West, and R. Drezek, Technol. Cancer Res. Treat. **3**, 33 (2004).
5. H. Cang, T. Sun, Z. Y. Li, J. Y. Chen, B. J. Wiley, Y. N. Xia, and X. D. Li, Opt. Lett. **30**, 3048 (2005).
6. A. Agrawal, S. Huang, A. W. H. Lin, M. H. Lee, J. K. Barton, R. A. Drezek, and T. J. Pfefer, J. Biomed. Opt. **11**, 041121 (2006).
7. A. L. Oldenburg, M. N. Hansen, D. A. Zweifel, A. Wei, and S. A. Boppart, Opt. Express **14**, 6724 (2006).
8. J. Oh, M. D. Feldman, J. Kim, H. W. Kang, P. Sanghi, and T. E. Milner, Lasers Surg. Med. **39**, 266 (2007).
9. D. C. Adler, S. W. Huang, R. Huber, and J. G. Fujimoto, Opt. Express **16**, 4376 (2008).
10. M. C. Skala, M. J. Crow, A. Wax, and J. A. Izatt, Nano Lett. **8**, 3461 (2008).
11. K. Sokolov, M. Follen, J. Aaron, I. Pavlova, A. Malpica, R. Lotan, and R. Richards-Kortum, Cancer Res. **63**, 1999 (2003).
12. D. P. O'Neal, L. R. Hirsch, N. J. Halas, J. D. Payne, and J. L. West, Cancer Lett. **209**, 171 (2004).
13. X. H. Huang, P. K. Jain, I. H. El-Sayed, and M. A. El-Sayed, Nanomedicine **2**, 681 (2007).
14. X. M. Yang, Radiology **243**, 340 (2007).
15. S. J. Oldenburg, J. B. Jackson, S. L. Westcott, and N. J. Halas, Appl. Phys. Lett. **75**, 2897 (1999).